Imaging the Microscopic Structure of Shear Thinning and Thickening Colloidal Suspensions

Xiang Cheng, *et al.*

Science **333**, 1276 (2011);
DOI: 10.1126/science.1207032

This copy is for your personal, non-commercial use only.

If you wish to distribute this article to others, you can order high-quality copies for your colleagues, clients, or customers by clicking here.

Permission to republish or repurpose articles or portions of articles can be obtained by following the guidelines here.

The following resources related to this article are available online at www.sciencemag.org (this infomation is current as of January 29, 2012):

Updated information and services, including high-resolution figures, can be found in the online version of this article at:
http://www.sciencemag.org/content/333/6047/1276.full.html

Supporting Online Material can be found at:
http://www.sciencemag.org/content/suppl/2011/08/31/333.6047.1276.DC1.html

A list of selected additional articles on the Science Web sites **related to this article** can be found at:
http://www.sciencemag.org/content/333/6047/1276.full.html#related

This article **cites 35 articles**, 2 of which can be accessed free:
http://www.sciencemag.org/content/333/6047/1276.full.html#ref-list-1

This article has been **cited by** 2 articles hosted by HighWire Press; see:
http://www.sciencemag.org/content/333/6047/1276.full.html#related-urls

This article appears in the following **subject collections:**
Medicine, Diseases
http://www.sciencemag.org/cgi/collection/medicine

Science (print ISSN 0036-8075; online ISSN 1095-9203) is published weekly, except the last week in December, by the American Association for the Advancement of Science, 1200 New York Avenue NW, Washington, DC 20005. Copyright 2011 by the American Association for the Advancement of Science; all rights reserved. The title *Science* is a registered trademark of AAAS.

and a displacement of -21 ± 3 fm, the contribution to the electrical polarization from this mode is calculated to be $P = 176\ \mu\text{C m}^{-2}$, around a quarter of the measured value (*1*) of $P \approx 600\ \mu\text{C m}^{-2}$. This establishes that ionic displacements of the symmetry and magnitude determined in our study account for the spontaneous ferroelectric polarization in $TbMnO_3$ to within an order of magnitude.

Our data decisively support microscopic models that attribute **P** to ionic displacements, but they also imply a need to include both symmetric and antisymmetric magnetic interactions in any such models. The technique introduced here should be applicable to other multiferroics and to the wider class of systems with complex order in the presence of magnetoelastic coupling.

References and Notes

1. T. Kimura *et al.*, *Nature* **426**, 55 (2003).
2. S.-W. Cheong, M. Mostovoy, *Nat. Mater.* **6**, 13 (2007).
3. M. Kenzelmann *et al.*, *Phys. Rev. Lett.* **95**, 087206 (2005).
4. T. Arima *et al.*, *Phys. Rev. Lett.* **96**, 097202 (2006).
5. F. Fabrizi *et al.*, *Phys. Rev. Lett.* **102**, 237205 (2009).
6. N. Aliouane *et al.*, *Phys. Rev. Lett.* **102**, 207205 (2009).
7. S. B. Wilkins *et al.*, *Phys. Rev. Lett.* **103**, 207602 (2009).
8. G. Lawes *et al.*, *Phys. Rev. Lett.* **95**, 087205 (2005).
9. O. Prokhnenko *et al.*, *Phys. Rev. Lett.* **98**, 057206 (2007).
10. R. Feyerherm, E. Dudzik, O. Prokhnenko, D. N. Argyriou, *J. Phys. Conf. Ser.* **200**, 012032 (2010).
11. A. B. Harris, *Phys. Rev. B* **76**, 054447 (2007).
12. H. Katsura, N. Nagaosa, A. V. Balatsky, *Phys. Rev. Lett.* **95**, 057205 (2005).
13. I. A. Sergienko, E. Dagotto, *Phys. Rev. B* **73**, 094434 (2006).
14. F. Bridges, C. Downs, T. O'Brien, I.-K. Jeong, T. Kimura, *Phys. Rev. B* **76**, 092109 (2007).
15. T. Kimura, G. Lawes, T. Goto, Y. Tokura, A. P. Ramirez, *Phys. Rev. B* **71**, 224425 (2005).
16. Y. Yamasaki *et al.*, *Phys. Rev. Lett.* **98**, 147204 (2007).
17. I. Cabrera *et al.*, *Phys. Rev. Lett.* **103**, 087201 (2009).
18. F. Fabrizi *et al.*, *Phys. Rev. B* **82**, 024434 (2010).
19. H. J. Xiang, S.-H. Wei, M.-H. Whangbo, J. L. F. Da Silva, *Phys. Rev. Lett.* **101**, 037209 (2008).
20. A. Malashevich, D. Vanderbilt, *Phys. Rev. Lett.* **101**, 037210 (2008).
21. R. F. Pettifer, O. Mathon, S. Pascarelli, M. D. Cooke, M. R. J. Gibbs, *Nature* **435**, 78 (2005).
22. N. Aliouane *et al.*, *Phys. Rev. B* **73**, 020102(R) (2006).
23. J. Strempfer *et al.*, *Phys. Rev. B* **78**, 024429 (2008).
24. See supporting material on *Science* Online.
25. S. W. Lovesey, S. P. Collins, *X-ray Scattering and Absorption by Magnetic Materials* (Clarendon, Oxford, 1996).

Acknowledgments: We thank C. Mazzoli and G. Pepellin for experimental assistance, and Y. Joly, A. Rogalev, and C. Vettier for fruitful discussions. Supported by the UK Engineering and Physical Sciences Research Council and the Royal Society. The data are stored at the European Synchrotron Radiation Facility.

Supporting Online Material

www.sciencemag.org/cgi/content/full/333/6047/1273/DC1
Materials and Methods
Figs. S1 and S2
Tables S1 and S2
References (*26–44*)

9 May 2011; accepted 28 July 2011
10.1126/science.1208085

Imaging the Microscopic Structure of Shear Thinning and Thickening Colloidal Suspensions

Xiang Cheng,[1]* Jonathan H. McCoy,[2] Jacob N. Israelachvili,[3] Itai Cohen[1]

The viscosity of colloidal suspensions varies with shear rate, an important effect encountered in many natural and industrial processes. Although this non-Newtonian behavior is believed to arise from the arrangement of suspended particles and their mutual interactions, microscopic particle dynamics are difficult to measure. By combining fast confocal microscopy with simultaneous force measurements, we systematically investigate a suspension's structure as it transitions through regimes of different flow signatures. Our measurements of the microscopic single-particle dynamics show that shear thinning results from the decreased relative contribution of entropic forces and that shear thickening arises from particle clustering induced by hydrodynamic lubrication forces. This combination of techniques illustrates an approach that complements current methods for determining the microscopic origins of non-Newtonian flow behavior in complex fluids.

Non-Newtonian fluid phenomena, such as shear thickening, are important for many natural and industrial processes (*1–3*) and are of interest to the general public, as exemplified by popular videos showing people running across swimming pools filled with such fluids (*4*). As a simple model system, colloidal suspensions of hard spheres in Newtonian fluids capture the essential features of many non-Newtonian behaviors, including shear thinning and thickening (*1*, *4–7*). Pioneering numerical simulations and experiments combining rheology with scattering techniques have done much to illuminate the microstructural origins of such phenomena (*4–14*). Nevertheless, numerous fundamental questions remain unresolved (*7*). For example, although shear thinning of suspensions is associated with formation of particle layers (*4*, *5*, *7*, *13*), whether such layering is necessary for thinning remains unresolved (*5*, *14*). In addition, while discontinuous shear thickening in concentrated suspensions is believed to result from the dilation and jamming of suspended particles (*15–19*), whether continuous shear thickening in moderately concentrated suspensions arises from order-to-disorder transitions (*13*, *14*) or from formation of particle clusters induced by lubrication hydrodynamics (*4*, *8*, *9*, *11*, *12*) remains controversial.

Resolving these questions is difficult in part because it is challenging to access single-particle dynamics over a range of length scales. Stokesian dynamics simulations typically studied small three-dimensional (3D) systems and therefore described local particle dynamics (*8*), whereas scattering experiments probed very large sample volumes and reported on average suspension structures (*10–12*). Moreover, scattering techniques have difficulty in resolving weak particle layering and heterogeneous ordering in moderately concentrated suspensions (*14*, *20*). Hence, there is a need for complementary experiments that bridge these limits by exploring large volumes with single-particle resolution and that can distinguish between proposed models. Here, by combining fast confocal microscopy (*20*, *21*) with simultaneous rheological measurements (*21*, *22*), we systematically correlate the real-space microstructure of concentrated hard-sphere suspensions with their flow properties.

Our samples consist of silica spheres, with diameter $2a = 0.96\ \mu\text{m}$ and polydispersity of 5%, suspended in a water-glycerin mixture with solvent viscosity $\eta_0 = 0.06$ Pa·s and matching refraction index. Fluorescein sodium salt is added so that particles appear as dots on a bright background. For our experiment volume fractions, $0.30 \le \phi < 0.48$, the suspension is a fluid at equilibrium, in accordance with phase behavior for hard spheres. Thus, under shear, suspension properties are determined solely by entropic and hydrodynamic forces.

Our shear cell mounts on a high-speed confocal microscope, which allows for imaging the 3D suspension structure (Fig. 1A) (*23*). The cell consists of a movable microscope cover slip as the bottom plate and a fixed 16-mm^2 square silicon wafer as the top plate. Both plates are flat on the particle length scale. Using set screws, the plates are made parallel to within 0.0075°. In our experiments, we use a plate separation of $h = 6.4 \pm 0.3\ \mu\text{m}$, which enables rapid 3D scanning of the entire sample. A piezoelectric actuator generates sinusoidal motion of the bottom plate with amplitude $A = 22\ \mu\text{m}$ and frequency $0 \le f \le 100$ Hz. Thus, our experiments are conducted at shear strain $\gamma \equiv A/h = 3.67$ and at shear rates $\dot{\gamma}_0 = 2\pi f(A/h)$ up to 2000. Throughout, we observe uniform shear gradients indicating weak

---

[1] Department of Physics, Cornell University, Ithaca, NY 14853, USA. [2] Department of Physics and Astronomy, Colby College, Waterville, ME 04901, USA. [3] Materials Research Laboratory and Department of Chemical Engineering, University of California, Santa Barbara, CA 93106, USA.

*To whom correspondence should be addressed. E-mail: xc92@cornell.edu

sedimentation due to density mismatch (*23*). The corresponding Péclet number Pe $\equiv \eta_0\dot{\gamma}_0 a^3/k_B T$, the dimensionless ratio comparing particle advection to diffusion, is 3200 at the maximum $\dot{\gamma}_0$. To measure 3D structures, stacks of images oriented parallel to the shear velocity–vorticity plane (*x*-*z*) are taken along the velocity gradient direction (*y*) (Fig. 1B). Finally, the upper plate is attached to a custom load cell that measures shear stress. Collectively, this apparatus functions as a "confocal rheoscope" (*21*, *22*).

Using this apparatus, we measure the frequency dependence of the dynamic shear viscosity, $\eta \equiv \tau_0/\dot{\gamma}_0$, and phase lag between stress and strain, δ. Here, τ_0 is the sinusoidal shear stress amplitude. These material properties are plotted versus Pe for suspensions with $\phi = 0.34 \pm 0.03$ and 0.47 ± 0.03 in Fig. 1C. The data show shear-thinning, Newtonian, and continuous shear-thickening regimes. In the thinning regime, where Pe ≤ 3.6, δ is smaller than π/2, indicating viscoelasticity. For 3.6 ≤ Pe ≤ 167, δ is nearly π/2 and η remains constant, signifying a viscous Newtonian response. For Pe ≥ 167, the high ϕ sample shear thickens and becomes more elastic, as indicated by a slight decrease in δ. Although we cannot resolve thickening in the low ϕ sample, our measurements are consistent with previous studies where very weak thickening is observed (*12*). Surprisingly, we find excellent agreement between our sample rheology for relatively small gaps and well-known trends for moderately concentrated bulk suspensions (*4*, *7*, *12*, *23*).

These rheological transitions correlate with changes in particle configurations. To quantify suspension structure, we generate a real-time 3D pair correlation function $g(\vec{r})$, defined as the probability of finding a particle at position $\vec{r}$ with respect to each particle center. We plot 2D cuts of $g(\vec{r})$ along three orthogonal planes centered at the origin (Fig. 1, D to G). At Pe = 0.036, the configuration is isotropic in the *x*-*z* plane as indicated by bright rings representing the first and second shells of neighboring particles (Fig. 1D). In the *y*-*z* and *x*-*y* planes, we observe a slight anisotropy due to particle layering induced by shear

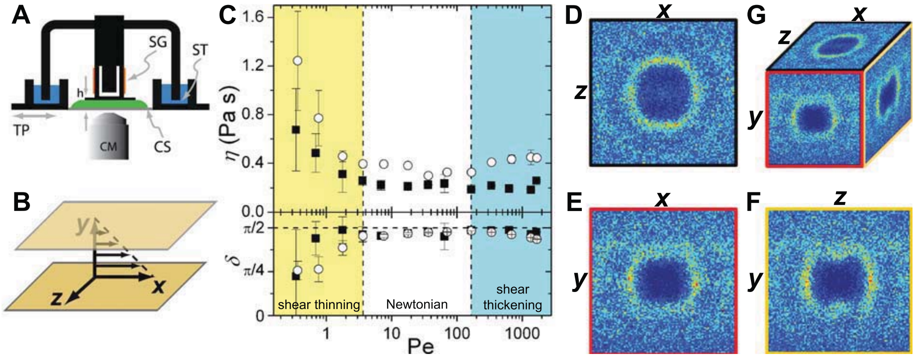

Fig. 1. (**A**) Setup. CM, confocal microscope; SG, strain gauge; CS, colloidal suspension; ST, solvent trap. (**B**) coordinates. (**C**) Colloidal suspension rheology versus Pe for ϕ = 0.34 (square) and ϕ = 0.47 (circle). Upper and lower panel show η and δ, respectively. Vertical dashed lines mark boundaries between rheological regimes. (**D** to **G**) $g(\vec{r})$ for ϕ = 0.34 sample at Pe = 0.036. (D to F) show cuts of $g(\vec{r})$ in the *z*-*x*, *x*-*y*, and *z*-*y* planes, and (G) indicates their orientation. Each plane is identified with a different bounding box color.

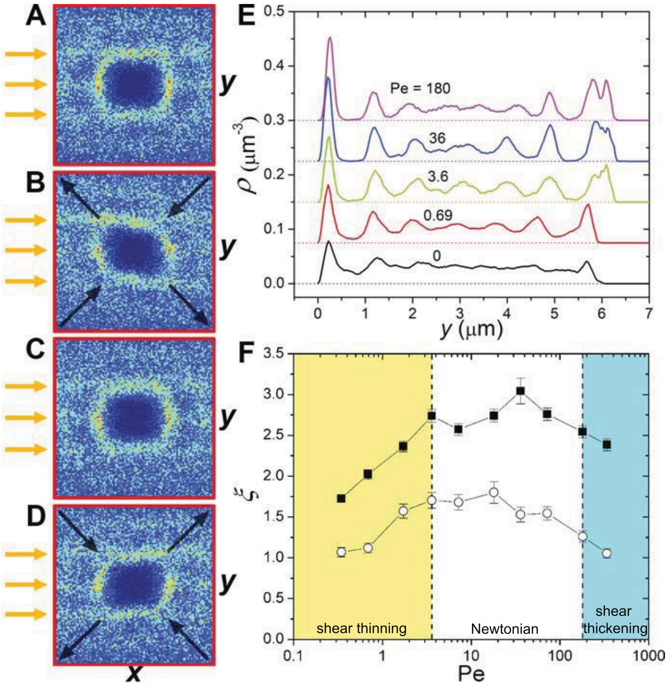

Fig. 2. (**A** to **D**) $g(x,y)$ for ϕ = 0.34 sample at Pe = 0.36 at a shear phase of ~π/2 (A), π (B), 3π/2 (C), and 2π (D) in an oscillation cycle. Shear-induced compression and extension are illustrated by black arrows. Layer structure is indicated by yellow arrows. (**E**) ρ(*y*) for ϕ = 0.34 sample. ρ(*y*) indicates the fraction of particles that are located in a slice of thickness *d* centered at *y*. Curves for different Pe are shifted vertically for clarity. (**F**) Order parameter, ξ, versus Pe for ϕ = 0.34 (square) and ϕ = 0.48 (circle) samples.

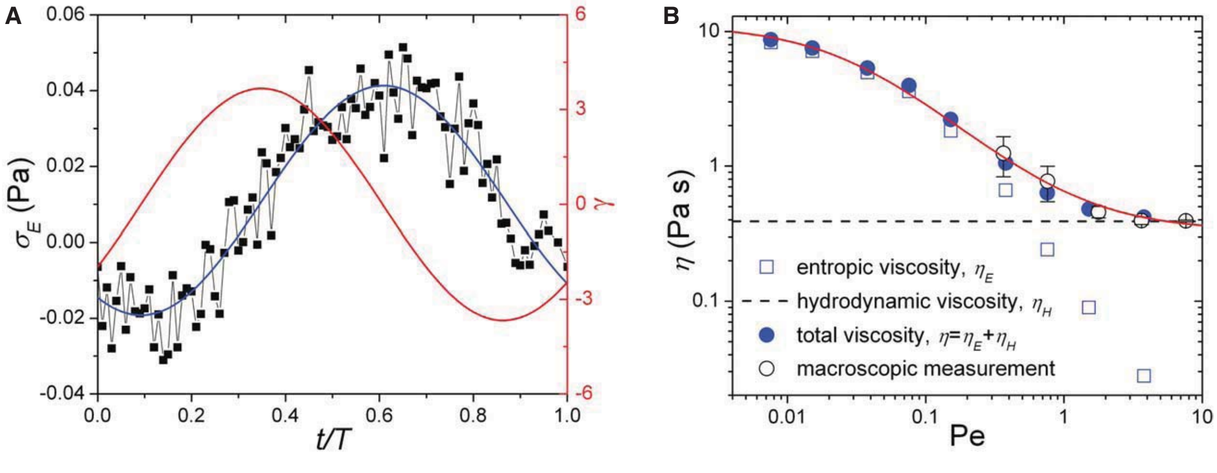

Fig. 3. (**A**) Entropic shear stresses, σ_E, calculated from $g(\vec{r})$ for ϕ = 0.47 at Pe = 0.015. The shear period *T* = 1/*f* = 5000 s. The blue line is a sinusoidal fit to σ_E. The red line is the corresponding shear strain. (**B**) Shear thinning induced by entropic stresses for ϕ = 0.47. The error bar for the entropic viscosity, $\eta_E = |\sigma_E/\dot{\gamma}|$, is smaller than the size of symbols. Red solid line is a fit to an empirical expression for shear thinning $\eta = \eta_\infty + \left(\frac{\eta_0 - \eta_\infty}{1 + b\mathrm{Pe}}\right)$ (*1*).

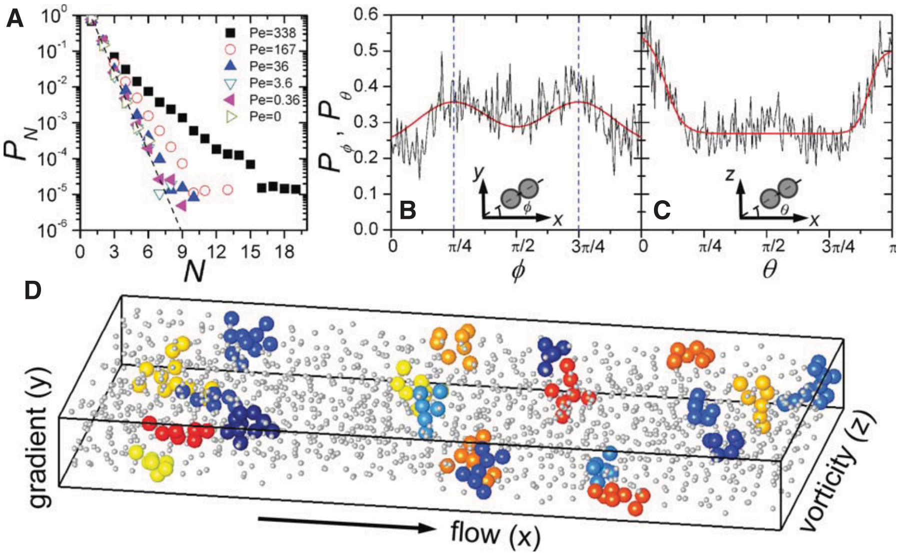

Fig. 4. Hydroclusters for $\phi = 0.47$ sample. (**A**) P_N, at different Pe. (**B** and **C**) Probability distribution of the neighboring particle orientations in clusters with $N \geq 6$. The orientation is projected onto the *x-y* plane (B) and the *x-z* plane (C), with corresponding angles defined in the insets. Red lines are guides to the eye. Results are averaged over a full cycle of shear. (**D**) Instantaneous real-space configuration of hydroclusters with $N \geq 6$ at shear phase 0.7. Different colors indicate different clusters. Particles outside the large clusters are drawn with smaller size for clarity. The boundary box is 31.2 by 15.4 by 3.1 μm^3.

plate confinement (Fig. 1, E and F) (*24*). More important, these patterns remain nearly constant throughout the oscillation cycle (movie S1). In contrast, with increasing Pe, while $g(x,z)$ and $g(y,z)$ remain constant, $g(x,y)$ exhibits strong oscillatory distortions as the suspension shear thins (Fig. 2, A to D, and movies S2 and S3). Simultaneously, the horizontal bands in $g(x,y)$ and $g(y,z)$ sharpen (Fig. 1, E and F; Fig. 2, A to D; and movies S1 to S3).

These structural signatures indicate both increased layering and the changing contribution of entropic stress to the total stress during thinning. The enhancement of layering is thought to decrease η by lowering dissipation due to collisions between particles (*5*, *7*, *13*, *14*). In our experiments, layering can be further shown by measuring the number density of particles along the *y* direction, $\rho(y)$, for different Pe (Fig. 2E). To quantify layering, we define the order parameter, $\xi(\mathrm{Pe}) = \frac{1}{N}\sum_{i=1}^{N}\frac{\rho_i(\mathrm{Pe})}{\rho_i(\mathrm{Pe}=0)}$, where ρ_i is the height of the *i*th peak relative to its adjacent valley in $\rho(y)$ and N is the number of layers. ξ increases throughout the shear-thinning regime, plateaus at the onset of the Newtonian regime, and decays before the shear-thickening regime (Fig. 2F). Additionally, we observe that as the suspension layers, particles form heterogeneous structure—crystalline patches—in the layers (*23*).

The increase and decrease in layering and in-layer structure is comparable at low and high Pe (Fig. 2F and fig. S3F). However, the magnitude of the η decrease during thinning is much larger than the η increase during thickening (Fig. 1C). This asymmetry indicates that layering does not account for large viscosity changes and points to an entropic origin for shear thinning (*4*, *5*, *7*, *8*).

Entropic contributions to the stresses are determined from shear-induced distortions in $g(\vec{r})$. At low Pe, small distortions indicate that Brownian motion is sufficiently rapid to restore the equilibrium suspension structure from entropically less favorable shear-induced configurations. At higher Pe, the larger distortions reflect the decreased contribution of entropic stresses relative to hydrodynamic stresses. As a result of hydrodynamic stresses, particles are squeezed together along the 45° major compressive axis and separated out along the 135° major extensional axis. Although evidence for this effect has been presented previously (*25*, *26*), here we quantitatively track distortion dynamics in real time over three decades in Pe (Fig. 2, B and D, and movies S2 and S3). We quantify the degree of distortion by integrating over the first peak of $g(\vec{r})$ and determine the entropic stress contribution (Fig. 3A) (*23*). During thinning, entropic contributions to the viscosity decrease monotonically (Fig. 3B, blue box). We assume that the hydrodynamic contribution is constant at low Pe and can be determined from the plateau viscosity in the Newtonian regime (Fig. 1C). Remarkably, we find that adding the constant hydrodynamic viscosity (Fig. 3B, dashed line) to the entropic viscosity completely accounts for the macroscopically measured shear-thinning data in Fig. 1C (Fig. 3B, blue disks). Entropic stresses also lead to viscoelasticity during thinning (*23*). Because entropic stresses result from distortions in equilibrium structure, we expect that layering only affects shear thinning through modification of equilibrium structures, which can, for example, arise from further confinement.

At higher Pe, entropic contributions to viscosity become negligible. Our data indicate that changes in layering and in-layer order do not alter the suspension viscosity in the thinning and Newtonian regimes. Therefore, we expect they do not contribute to shear thickening either. Consistent with this interpretation, we find that decreased layering and in-layer structure are not correlated with the onset of shear thickening (Fig. 2F and fig. S3F). Because our volume fractions are well below those needed for jamming or glassy behavior, the system is dominated by hydrodynamic interactions rather than frictional contacts between particles (*15*–*19*). These observations are consistent with the prediction that hydroclusters—groups of particles whose relative motions are restricted by lubrication stresses—are responsible for shear thickening (*4*, *8*, *9*).

Enhanced hydrodynamic coupling between particles in the thickening regime can be observed in our confocal movies by studying the increasingly restricted nonaffine particle motions (movies S4, S5, and S6) (*23*). To detect hydroclusters, we perform a cluster analysis to identify particles that are close and display large nonaffine movements (*23*). We define a threshold interparticle distance D for including a particle in a cluster and determine the probability, P_N, of obtaining a cluster with N particles. D is chosen as the largest distance that leads to exponential decay in P_N for stationary suspensions, and its value is roughly one particle diameter (*23*). The exponential decay of P_N persists until the onset of thickening (Fig. 4A). As the suspension thickens, we measure a greater probability for obtaining large clusters. Furthermore, we find that neighboring particles within clusters preferentially align along the 45° and 135° axis in the *x-y* plane (Fig. 4B) and along the flow direction in the *x-z* plane (Fig. 4C). These cluster morphologies are consistent with those predicted by simulations (*27*) and account for the slight elastic response. Thus, using these techniques, we identify and visualize hydroclusters as the origin of shear thickening in colloidal suspensions (Fig. 4D).

Our measurements demonstrate the coupling between microstructure and macroscopic flow behaviors in colloidal suspensions. They provide experimental evidence for the entropic origin of shear thinning and the hydrodynamic coupling that leads to thickening. The combination of imaging techniques and force measurements presented illustrates a powerful approach for investigating the microscopic origins of non-Newtonian flows in structured fluids relevant for processes ranging from lubrication to biorheology (*1*, *28*).

References and Notes

1. R. G. Larson, *The Structure and Rheology of Complex Fluids* (Oxford Univ. Press, New York, 1999).
2. Y. Dzenis, *Science* **304**, 1917 (2004).
3. P. Beiersdorfer, D. Layne, E. W. Magee, J. I. Katz, *Phys. Rev. Lett.* **106**, 058301 (2011).
4. N. J. Wagner, J. F. Brady, *Phys. Today* **62**, 27 (2009).
5. J. J. Stickel, R. L. Powell, *Annu. Rev. Fluid Mech.* **37**, 129 (2005).

6. J. Vermant, M. J. Solomon, *J. Phys. Condens. Matter* **17**, R187 (2005).
7. J. M. Brader, *J. Phys. Condens. Matter* **22**, 363101 (2010).
8. D. R. Foss, J. F. Brady, *J. Fluid Mech.* **407**, 167 (2000).
9. J. R. Melrose, R. C. Ball, *J. Rheol. (N.Y.N.Y.)* **48**, 961 (2004).
10. H. M. Laun *et al.*, *J. Rheol. (N.Y.N.Y.)* **36**, 743 (1992).
11. B. J. Maranzano, N. J. Wagner, *J. Chem. Phys.* **117**, 10291 (2002).
12. D. Kalman, N. J. Wagner, *Rheol. Acta* **48**, 897 (2009).
13. R. L. Hoffman, *J. Colloid Interface Sci.* **46**, 491 (1974).
14. R. L. Hoffman, *J. Rheol. (N.Y.N.Y.)* **42**, 111 (1998).
15. C. B. Holmes, M. E. Cates, M. Fuchs, P. Sollich, *J. Rheol. (N.Y.N.Y.)* **49**, 237 (2005).
16. D. Lootens, H. van Damme, Y. Hémar, P. Hébraud, *Phys. Rev. Lett.* **95**, 268302 (2005).
17. A. Fall, N. Huang, F. Bertrand, G. Ovarlez, D. Bonn, *Phys. Rev. Lett.* **100**, 018301 (2008).
18. E. Brown *et al.*, *Nat. Mater.* **9**, 220 (2010).
19. E. Brown, H. M. Jaeger, Preprint at http://arxiv.org/abs/1010.4921 (2010).
20. Y. L. Wu, D. Derks, A. van Blaaderen, A. Imhof, *Proc. Natl. Acad. Sci. U.S.A.* **106**, 10564 (2009).
21. L. Isa, R. Besseling, A. B. Schofield, W. C. K. Poon, *Adv. Polym. Sci.* **236**, 163 (2010).
22. K. M. Schmoller, P. Fernández, R. C. Arevalo, D. L. Blair, A. R. Bausch, *Nat. Commun.* **1**, 134 (2010).
23. Materials and methods are available as supporting material on *Science* Online.
24. C. R. Nugent, K. V. Edmond, H. N. Patel, E. R. Weeks, *Phys. Rev. Lett.* **99**, 025702 (2007).
25. F. Parsi, F. Gadala-Maria, *J. Rheol. (N.Y.N.Y.)* **31**, 725 (1987).
26. C. Gao, S. D. Kulkarni, J. F. Morris, J. F. Gilchrist, *Phys. Rev. E Stat. Nonlin. Soft Matter Phys.* **81**, 041403 (2010).
27. J. F. Brady, G. Bossis, *J. Fluid Mech.* **155**, 105 (1985).
28. M. Urbakh, J. Klafter, D. Gourdon, J. Israelachvili, *Nature* **430**, 525 (2004).

Acknowledgments: We thank T. Beatus, Y.-C. Lin, J. Brady, L. Ristroph, and N. Wagner for useful discussions. This research was supported by grants from NSF Civil, Mechanical, and Manufacturing Innovation, Division of Materials Research (DMR), and DMR Materials Research Science and Engineering Centers, and in part by award KUS-C1-018-02 from King Abdullah University of Science and Technology (KAUST). J.N.I. was supported by the U.S. Department of Energy, Division of Materials Sciences and Engineering under award DE-FG02-87ER-45331.

Supporting Online Material

www.sciencemag.org/cgi/content/full/333/6047/1276/DC1
Materials and Methods
SOM Text
Figs. S1 to S7
Movies S1 to S6
References (*29*–*40*)

15 April 2011; accepted 15 July 2011
10.1126/science.1207032

Traffic Jams Reduce Hydrolytic Efficiency of Cellulase on Cellulose Surface

Kiyohiko Igarashi,[1]*† Takayuki Uchihashi,[2,3,4]* Anu Koivula,[5] Masahisa Wada,[1,6] Satoshi Kimura,[1,6] Tetsuaki Okamoto,[1,2] Merja Penttilä,[5] Toshio Ando,[2,3,4] Masahiro Samejima[1]

A deeper mechanistic understanding of the saccharification of cellulosic biomass could enhance the efficiency of biofuels development. We report here the real-time visualization of crystalline cellulose degradation by individual cellulase enzymes through use of an advanced version of high-speed atomic force microscopy. *Trichoderma reesei* cellobiohydrolase I (*Tr*Cel7A) molecules were observed to slide unidirectionally along the crystalline cellulose surface but at one point exhibited collective halting analogous to a traffic jam. Changing the crystalline polymorphic form of cellulose by means of an ammonia treatment increased the apparent number of accessible lanes on the crystalline surface and consequently the number of moving cellulase molecules. Treatment of this bulky crystalline cellulose simultaneously or separately with *T. reesei* cellobiohydrolase II (*Tr*Cel6A) resulted in a remarkable increase in the proportion of mobile enzyme molecules on the surface. Cellulose was completely degraded by the synergistic action between the two enzymes.

Biorefining encompasses production of fuels, power, heat, and value-added chemicals by appropriate conversion of lignocellulosic feedstocks. This prospect offers many advantages, including diminished carbon dioxide emission, productive use of renewable nonfood crops or inedible waste products, and reduction of petroleum use. One of the bottlenecks to widespread biorefining application is the enzymatic hydrolysis of the cellulosic raw material into sugars. In attempts to maximize efficiency and reduce costs, many studies on both individual cellulases and enzyme cocktails have been carried out (*1*). Various pretreatment methods have also been examined to increase the amount of sugar generated from cellulosic biomass with reduced enzyme loading and energy consumption, aiming at the development of commercially viable bioprocesses. It is generally recognized that one of the problems in cellulose hydrolysis is the slowdown of enzyme action with time and conversion (*2*, *3*). Cellulose is a major component of plant cell walls, accounting for almost half of their net weight. Cell wall cellulose typically has ~70% crystallinity, suggesting that approximately one-third of net cellulosic biomass consists of natural crystalline cellulose, which is generally called cellulose I (*4*). Because cellulose chains have stable β-1,4-glucosidic bonds and each chain is also stabilized by intra- and intermolecular hydrogen bonds, cellulose I is quite resistant not only to chemical hydrolysis but also to enzymatic degradation (*5*).

The industrially important cellulolytic ascomycete fungus *Trichoderma reesei* (anamorph of *Hypocrea jecorina*) secretes two extracellular cellobiohydrolases (CBHs), which are cellulases that can hydrolyze glycosidic linkages particularly at a crystalline surface, and form cellobiose (β-1,4-glucosidic dimer) as a major product from cellulose I (*6*). The two *T. reesei* CBHs hydrolyze crystalline cellulose from the reducing and nonreducing ends, respectively (*7*). These enzymes have a similar two-domain organization: The cellulose-binding domain (CBD), which is categorized into carbohydrate-binding module (CBM) family 1, contributes to adsorption on the insoluble substrate, and the cellulose-hydrolyzing catalytic domain (CD) catalyzes cleavage of glycosidic bonds. The two *T. reesei* cellobiohydrolase CDs have different types of folds. The CD of CBH I belongs to the glycoside hydrolase (GH) family 7, and the CD of CBH II belongs to the GH family 6, as listed on the Carbohydrate-Active enZyme (CAZy) server (*8*), and thus, the two enzymes are called *Tr*Cel7A and *Tr*Cel6A, respectively. In both cellobiohydrolases, the catalytic amino acids are located in a relatively long tunnel formed by surface loops extending from the central fold of the CD (*9*, *10*). We previously visualized the linear movement of wild-type and isolated CD on cellulose I_α using high-speed atomic force microscopy (HS-AFM); the data suggested that the sliding movement of wild-type *Tr*Cel7A reflects the processive degradation of the cellulose chain by catalysis at the CD and requires initial recognition of the cellulose chain. The chain recognition involves the tryptophan residue W40 at the entrance of the *Tr*Cel7A active site tunnel (*11*).

In the present study, we succeeded in enhancing the temporal and spatial resolutions by using a laboratory-built HS-AFM with extensive improvements over the version reported previously (*12*), and we were able to visualize the movement of *Tr*Cel7A molecules on crystalline cellulose in detail. Enzyme molecules sliding

---

[1] Department of Biomaterial Sciences, Graduate School of Agricultural and Life Sciences, University of Tokyo, Bunkyo-ku, Tokyo 113-8657, Japan. [2] Department of Physics, Kanazawa University, Kanazawa 920-1192, Japan. [3] Bio-AFM Frontier Research Center, College of Science and Engineering, Kanazawa University, Kakuma-machi, Kanazawa 920-1192, Japan. [4] Core Research for Evolutional Science and Technology, Japan Science and Technology Agency, Sanbon-cho, Chiyoda-ku, Tokyo 102-0075, Japan [5] VTT Technical Research Centre of Finland, Post Office Box 1000, FI-02044 VTT, Finland. [6] Department of Plant and Environmental New Resources, College of Life Sciences, Kyung Hee University, 1, Seocheon-dong, Giheung-ku, Yongin-si, Gyeonggi-do 446-701, Republic of Korea.

*These authors contributed equally to this work.

†To whom correspondence should be addressed. E-mail: aquarius@mail.ecc.u-tokyo.ac.jp (K.I.)